Table S1 | Experimental setup parameters. Details of casting runs and controlled process conditions.

Parameter	**Range / Values**
Melt temperature	1250–1350 °C
Wheel speed	8–12 rpm
Nozzle geometry	Straight slit / tapered slit
Slit width	25–30 mm
Wheel diameter	296 mm

Table S2 | Ridge analysis metrics across stable vs unstable runs.

Condition	**Ridge density (1/mm)**	**Mean ridge width (mm)**	**Surface unevenness (%)**
Stable	4–5	0.25 ± 0.02	10–15%
Unstable	6–9	0.30 ± 0.05	40–60%

Table S3 | Thermal profile metrics comparing stable vs unstable runs.

Condition	**Mean ΔT across foil (°C)**	**Edge-to-centre ∇T ratio**
Stable	20–25 °C	≈1.0
Unstable	40–60 °C	1.5–2.0

Table S4 | Hyperparameters for XGBoost and deep-learning fusion models.

Model	Parameter	Value
XGBoost	Learning rate	0.05
XGBoost	Max depth	6
XGBoost	Estimators	500
XGBoost	Regularisation λ	1.0
DL Fusion	CNN backbone	ResNet-18
DL Fusion	Fusion layer	Transformer encoder
DL Fusion	Dropout	0.3
DL Fusion	Optimiser	Adam, lr=1e-4

Table S5 | Ablation study results. Prediction error (MAE for gap, error for flow proxy) under selective removal of feature categories.

Condition	Gap MAE (mm)	Flow error (% change, optical flow velocity)
All features	0.010	0.18 %
–Ridge	0.014	0.28 %
–Reflection	0.0112	0.20 %
–Thermal	0.0120	0.23 %

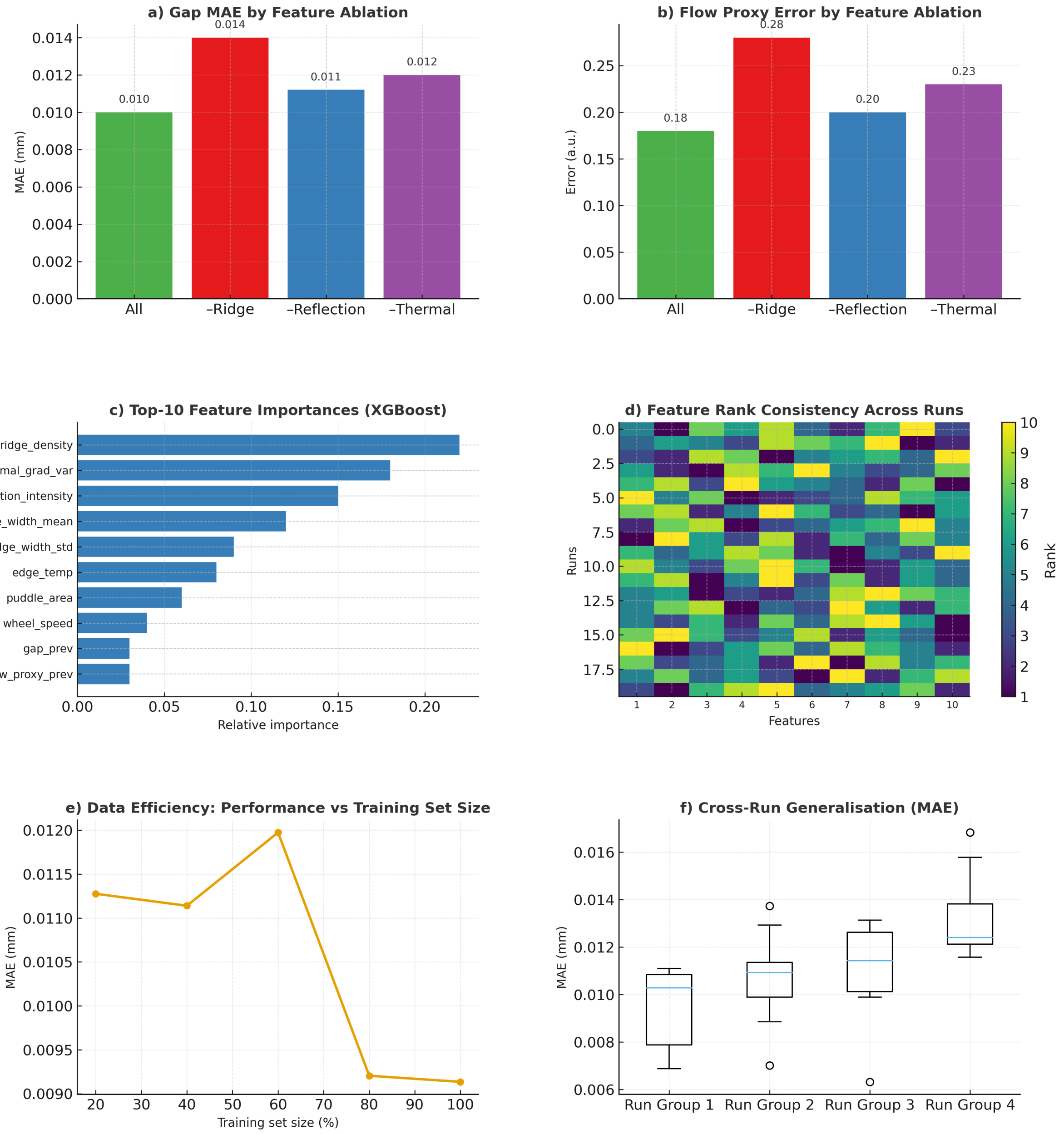

a) Gap MAE by Feature Ablation

b) Flow Proxy Error by Feature Ablation

c) Top-10 Feature Importances (XGBoost)

d) Feature Rank Consistency Across Runs

e) Data Efficiency: Performance vs Training Set Size

f) Cross-Run Generalisation (MAE)

Supplementary Figure 6 | Ablation studies and feature contribution to predictive performance.

(a) Gap prediction error (MAE) under selective feature ablation shows that removal of ridge descriptors increases error by ≈40%, underscoring their central role. Reflection and thermal features contribute moderately, but all feature groups provide complementary value.

(b) Flow proxy error rises sharply when ridge descriptors are excluded, confirming their joint contribution with reflection and thermal cues to flow stability prediction.
(c) XGBoost feature-importance ranking across the top 10 descriptors highlights ridge density and thermal-gradient variance as consistently dominant, followed by reflection

intensity and ridge-width statistics.

(d) Heatmap of feature rank consistency across 20 independent runs demonstrates robustness, with ridge-related features dominating predictive influence regardless of run-to-run variability.

(e) Data efficiency curve (performance vs training set size) shows steep gains in accuracy with modest dataset fractions, followed by saturation, illustrating efficient learning from relatively small experimental datasets.

(f) Cross-run generalisation analysis (boxplots of MAE) confirms stable performance across diverse experimental conditions, with only minor variability between run groups.

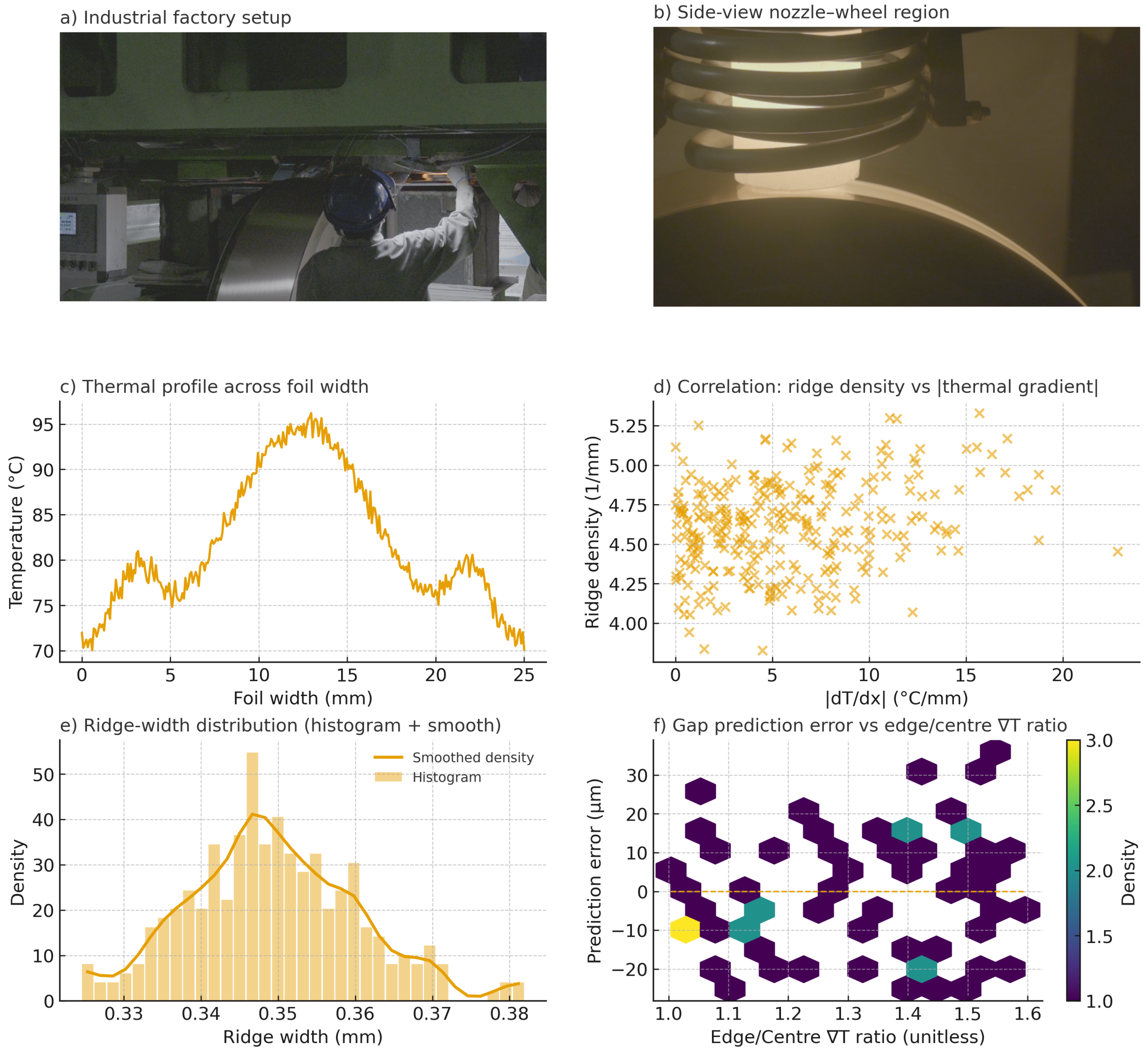

Supplementary Figure 7 | Industrial factory context and advanced analytics of planar-flow casting.

(a) Photograph of the industrial planar-flow casting line used for amorphous steel foil production.

(b) Side-view of the nozzle–wheel region highlighting the melt jet impingement and foil emergence during high-speed casting.

(c) Thermal profile across foil width from infrared monitoring, showing non-uniform edge heating.

(d) Correlation between ridge density and |thermal gradient| across runs.

(e) Ridge-width distribution across casts, shown as histogram with smoothed density overlay.
(f) Gap prediction error versus edge-to-centre temperature gradient ratio, presented as hexbin density map.

Supplementary_Video_S1_FoilTracking.mp4

Automated ridge and event-tracking sequence showing foil motion and ridge detection during planar-flow casting.

Supplementary_Video_S2_ThermalGradientAnalysis.mp4

Combined visualisation of thermal-gradient evolution and ridge-width variation across the foil, illustrating the link between heat imbalance and surface instability.